

Effects of Upstream Flow Conditions on Runner Pressure Fluctuations

K. Amiri^{1†}, B. Mulu², M. Raisee³ and M. J. Cervantes^{1,4}

¹ Department of Engineering Science and Mathematics, Division of Fluid and Experimental Mechanics, Luleå University of Technology, Luleå, 971 87, Sweden.

² Vattenfall Research and Development, Älvkarleby, 814 70, Sweden.

³ Mechanical Engineering Department, University of Tehran, 14155-6448, Tehran, Iran.

⁴ Department of Energy and Process Engineering, Water Power Laboratory, Norwegian University of Science and Technology, Trondheim, 7491, Norway.

†Corresponding Author Email: Kaveh.amiri@ltu.se

(Received September 20, 2016; accepted February 8, 2017)

ABSTRACTS

The rotor-stator interaction and the corresponding pressure fluctuations represent one of the sources of pressure and load fluctuations on the rotating parts of rotating machineries. The high-Reynolds flow is subject to rotation in the comparably large vaneless space of axial turbines, causing wake interaction and wake dissipation in this region. This increases the level of flow complexity in this region. This study examined the effect of the flow condition entering the spiral casing on the flow condition within the distributor and the runner and the physical source of pressure fluctuations exerted on the runner of a Kaplan turbine model. Simulations were performed within the water supply system, including the upstream tank, penstock, and the Francis turbines, the level of entering the spiral casing; the results were compared with laser Doppler anemometry (LDA) results. The results were considered as the inlet boundary condition for simulation of the turbine model from the spiral inlet to the draft tube outlet to investigate the flow condition within the distributor and the runner. The CFD simulations showed that the water supply system induces inhomogeneity to the velocity distribution at the spiral inlet. However, the flow condition does not affect the pressure fluctuations exerted on the runner blades due to the rotor-stator interactions. Moreover, the dominant frequencies exerted on the runner blades were accurately approximated although the amplitudes of the fluctuations were underestimated.

Keywords: Kaplan turbine; Rotor-stator interaction; LDA; CFD.

NOMENCLATURE

f^*	dimensionless frequency	U_r	radial velocity in turbine coordinates
Q	flow rate	U_θ	tangential velocity in turbine coordinates
r^*	dimensionless radial location	V	velocity
U^*	dimensionless Axial velocity	θ	angular position
U_{ax}	axial velocity in turbine coordinates		

1. INTRODUCTION

The constant increase in demand for electricity has encouraged hydropower production companies to manufacture hydraulic turbines with higher output power and higher efficiency. In this context, manufacturing turbines with a wider operating range is desirable due to the fast growth rate of intermittent electricity generation systems and the use of hydraulic turbines in grid regulation. The responsibility of grid regulation increases transient and off-design operations in hydraulic turbines. This responsibility, together with the demand for

manufacturing turbines with higher output power, contributes to increasing the level of fluctuations exerted on the rotating parts of turbines, i.e., the runner, runner bearings and bearings of the runner blades of Kaplan turbines. Among all fluctuation sources, the rotor-stator interaction is of particular importance because it always induces pressure fluctuations in the runner during both the steady-state and transient operation of turbines.

The rotor-stator interaction in Francis turbines has been subject of various experimental investigations. Farhat *et al.* (2002) performed pressure

measurements on the blades of a pump turbine model to measure pressure fluctuations exerted on the rotating parts of the turbine. The pressure fluctuations exerted on the runner blades of a Francis model and its corresponding prototype were investigated by Kobro (2010). Trivedi *et al.* (2013, 2015a; 2016; 2015b) used the same model as Kobro (2010) for pressure measurements on the runner blades during steady-state operation and load variations. In these studies, frequency analysis was performed on the acquired data to clarify the dominant frequencies exerted on different parts of the blades. The results indicated the presence of fluctuating forces at the runner frequency that could be due to the likely introduction of structural asymmetry in the manufacturing process, induction of flow asymmetries by the draft tube bend located downstream or an asymmetry in the flow entering the runner provided by the water supply system. However, the source of the disturbances was not clarified.

Although there is a close rotor-stator interaction in Francis turbines, the degree of interaction is lower in the case of axial turbines because of the comparably large vaneless space. The flow in this region is subject to rotation and wake dissipation, which make the flow condition more complicated compared to that in Francis turbines. Pressure measurements on the runner of a Kaplan model, known as Porjus U9, showed clear flow asymmetries at the distributor outlet (Amiri *et al.* 2015). Such asymmetry caused pressure fluctuations on the runner with respect to the runner frequency and guide vanes (GVs) passing frequency. However, the main source of pressure fluctuations cannot be determined by pressure measurements due to the limited information provided by such point measurements.

Numerical simulations can be used as a complementary tool for investigating flow conditions within a turbine conduit. They provide detailed information about the velocity and pressure fields over the computational domain and are proven to be capable of predicting different flow phenomena in axial hydraulic turbines. Petit *et al.* (2010) simulated stationary parts of a Kaplan turbine model using steady-state incompressible RANS models. The simulation domain consisted of stationary parts located upstream of the runner, including the penstock, spiral casing, and the distributor. Simulations have also been performed to study the flow condition inside the draft tube separately. The results were validated using LDA measurements performed at the spiral inlet, within the spiral, and within the draft tube. Javadi and Nilsson (2014) simulated the GV, runner and draft tube of the turbine model using RANS equations with the RNG $k-\epsilon$ turbulence model to perform more detailed investigations of the flow condition within the runner and the draft tube. Liu *et al.* (2009) performed an unsteady numerical simulation of a Kaplan turbine model to investigate pressure fluctuations in the distributor and the draft tube of the model. Liu *et al.* (2008) simulated both the model of the Kaplan turbine used in the previous

study and the corresponding prototype. They also studied the effect of the fluid-solid coupling during the numerical simulations on the pressure fluctuations of the prototype Kaplan turbine. Wu *et al.* (2012) extended the previous studies by performing numerical simulations during on-cam and off-cam operations of the Kaplan turbine model and its prototype to perform a similarity study between the two cases. Vu *et al.* (2010) and Nicolle *et al.* (2010) investigated the effect of non-homologous blade geometries on the overall performance and flow condition within a propeller turbine model (named AxialT) and a Francis turbine. A numerical simulation of the flow in the complete model of the AxialT turbine was performed to investigate circumferential non-uniformities in the distributor and at the stay vanes inlet of an axial turbine by Gagnon *et al.* (2008). The results showed that flow non-uniformities are initiated at the admission duct. The simulation results were validated against LDA and PIV measurements to investigate the performance of the numerical models. Mulu *et al.* (2015) performed transient flow simulations on a Kaplan turbine model while operating at the best efficiency point (BEP), investigating 3D flows formed near the hub region and propagating downstream. Liu *et al.* (2010) solved the equation of rotational motion of a runner, the continuity equation and unsteady RANS equations with the RNG $k-\epsilon$ turbulence model to simulate the runaway transient operation of a Kaplan turbine model. Fortin *et al.* (2014) analyzed the AxialT turbine during runaway, with a special focus on the effect of the runaway on the pressure pulsations exerted on the runner. Compressible and incompressible simulations were performed to assess the impact of the weakly compressibility of water on the dynamic behavior of the flow. During the simulation, the variations in the head and the rotational speed acquired during the measurements were considered as input to the CFD solver to eliminate the associated potential source of error that can have a dramatic effect on the flow simulations. Kolsek *et al.* (2006) proposed a novel tool for performing mesh generation that changes over time to take into account significant geometrical changes in the computational domain. The proposed method involves a moving computational mesh, which is a practically valuable method for simulating transient operating conditions in turbines involving GV and/or runner blade movements. The method was implemented to simulate the shut-down of a bulb turbine as a complex case incorporating movements of both GV and runner blades. Nennemann and Vu (2007) simulated the GV and runner of a Kaplan turbine prototype to predict the effects of cavitation on the runner and discharge ring in the case study. More recently, Kumar and Bhingole (2015) implemented CFD methods to analyze the combined effect of cavitation and slit erosion on a Kaplan turbine.

The foregoing review of previous studies demonstrates the applicability of unsteady RANS methods in predicting different phenomena occurring within the conduit of axial turbines, such as separation, wake propagation, transient

operations, and cavitation. However, the performance of numerical simulations in studying such flows is still under investigation. The fact that most numerical simulations investigating the flow condition inside hydraulic turbines are accompanied by experimental results for validation indicates that more investigations on the numerical simulation of hydraulic turbines are required to increase the reliability of the technique. More specifically, unlike in the case of Francis turbines, the interaction between the rotor and stator has not been deeply investigated in the case of Kaplan turbines. Although there is a close rotor-stator interaction in Francis turbines, the level of interaction is lower in the case of axial turbines because of the comparably large vaneless space. The flow in this region is subject to rotation and wake dissipation, which makes the numerical simulations more challenging compared with those of Francis turbines. The mesh quality, mesh element size, numerical dissipation and the effect of the mandatory use of general grid interface (GGI) between the stages should be controlled, and their effect on simulation of rotor-stator interaction should be considered.

The main purpose of the current study was to conduct a numerical investigation of the pressure fluctuations exerted on the runner of the Porjus U9 Kaplan model due to the interaction between the runner and the spiral casing/distributor of the model. Experimental investigations of the pressure fluctuations exerted on the runner of the Kaplan model showed clear flow asymmetries delivered to the runner of the model (Amiri *et al.*, 2015). The source and location of the asymmetry were not identified by the measurements. The source of the asymmetry could be the flow condition at the spiral inlet, the geometry of the spiral casing or the distributor. The whole turbine model, starting from the upper tank of the test rig to the draft tube outlet, was simulated using the SAS-SST turbulence model. The model was divided into two sub-domains, and flow was simulated within each domain. The first domain included the inlet of the upstream tank to the outlet of the spiral casing, and the second included the inlet of the spiral casing to the draft tube outlet. The results of the first simulation were used as the inlet boundary condition for simulating the second domain to investigate the effect of the flow condition at the inlet of the spiral casing on the fluid structure interaction. The results of the second domain clarified the source and the location of the asymmetries at the distributor outlet. The results were compared with LDA measurement results at the entrance of the spiral casing and pressure measurements performed on the runner blades.

2. TEST CASE

A 1:3.1-scale model of a Kaplan turbine known as Porjus U9 was selected as the test case for numerical simulations and experimental investigations. The turbine is composed of a penstock to mimic the flow condition at the power plant, a spiral casing, a distributor consisting of 18 stay vanes and 20 GVs, a Kaplan runner with 6

blades, and an elbow-type draft tube following the runner. The model has a runner diameter of 0.5 m. It was tested at the head and rotational speed of 7.5 m and 696.3 rpm, respectively, to ensure kinematic similarity between the model and the prototype during the measurements. The BEP of the turbine was selected for this study. The corresponding GV angle for this operating point is 26.5°, resulting in a flow rate of 0.7 m³/s through the model.

The model measurements were performed at the Vattenfall R&D model test facility in Älvkarleby, Sweden. The test rig is a closed-loop system designed for testing Kaplan, bulb and Francis turbines. Fig. 1 shows the test rig with the Porjus U9 model installed between the upstream high-pressure tank and the downstream low-pressure one. The turbine head can be controlled by setting the power of the test rig pumps and independent adjustment of the pressure inside the upstream and downstream tanks. The ability to adjust the pressure inside each tank independently allows for adjustments of the turbine head as well as the absolute pressure within the draft tube to either trigger or prevent cavitation. Measurements were performed under cavitation-free conditions. The uncertainty in the flow rate and that in the hydraulic efficiency measurements were $\pm 0.13\%$ and $\pm 0.18\%$, respectively; see Mulu *et al.* (2012) for additional information about the test rig.

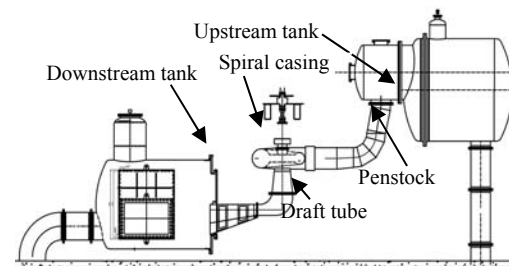


Fig. 1. Schematic of the U9 model installed on the test rig.

3. EXPERIMENTAL MEASUREMENTS

Preliminary velocity measurements at the inlet of the spiral casing showed a complex flow condition at the measurement section, which may affect its performance (Mulu and Cervantes, 2010). In this study, velocity measurements were performed at the inlet of the spiral casing to obtain the inlet boundary condition for the numerical simulation of the turbine. The goal of the simulations was to investigate the effect of the flow condition at the inlet of the spiral casing on the performance of the spiral casing in providing symmetrical flow to the runner.

The spiral casing was made of a stainless steel pipe with an inner radius of 316 mm at its inlet. A 290 mm long Plexiglas pipe was installed between the penstock and the spiral casing to provide the required optical access for LDA measurements; see Fig. 2. The local index-matching box shown in 0 Fig. 2 was used to improve the measurement

quality. A specific index-matching box consisting of a Plexiglas pipe with an axis normal to the axis of the penstock and high-quality glass with a diameter of 100 mm was manufactured to measure axial and tangential velocities along arbitrary radii. One end of the Plexiglas pipe was shaped to match the penstock pipe to prevent water leakage. The glass was mounted on the other side of the Plexiglas pipe. The space inside the index-matching box was filled with water as the index-matching liquid.

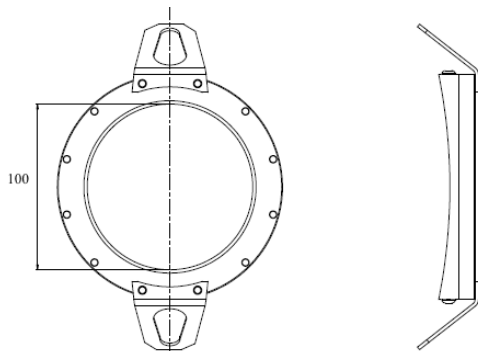
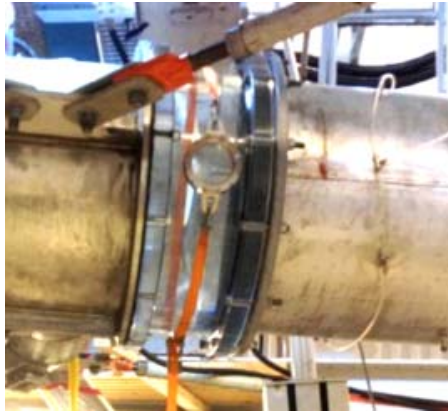


Fig. 2. Inlet section of the spiral casing together with a sketch of the index-matching box.

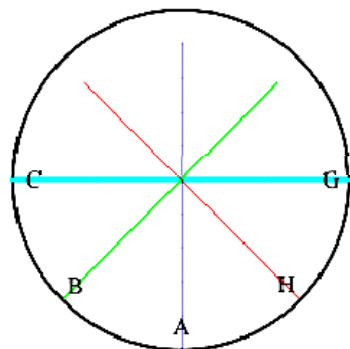


Fig. 3. Location of the velocity measurements at the inlet of the spiral casing.

The measurements at the inlet of the spiral casing were performed along five different radii separated by 45°. The measurement locations are presented in Fig. 3. The limited power of the lasers restricted the possible measurement depth in water to approximately 430 mm. Hence, measurements

along C-G were performed from both sides of the pipe to obtain the full velocity profile along the diameter. However, measurements from the top half of the pipe were not possible because of practical limitations.

A two-component LDA system with an 85 mm optical fiber probe from Dantec was used to measure the velocity distribution at different locations of the turbine. A front lens with a 600 mm focal length was used for the measurements. The measuring volume sizes based on the e-2 Gaussian intensity cut-off point were estimated to be $2.229 \times 0.140 \text{ mm}^2$ and $2.426 \times 0.147 \text{ mm}^2$ for the axial and tangential components, respectively. The measurements were performed in burst and coincidence mode, recording one pair of velocities (axial and tangential) for each passing particle during the measurements. The total sampling time was set to 240 s for each measurement point, which showed a good statistical convergence of the acquired signals. This sampling time corresponded to 100,000-200,000 bursts at each measurement location function of the position.

Pressure measurements were performed on the runner blades of the model while the turbine was operating at the BEP. Six piezo-resistive miniature pressure sensors manufactured by Kulite (LL-80 series) were flush mounted on the pressure side of one runner blade. The sensors were located on the vertices of a net formed by the imaginary circles passing through 1/3 and 2/3 of the blade span and 1/4, 1/2 and 3/4 of the blade chord lines. Six pressure sensors were also installed on the suction side of the adjacent blade to investigate the flow condition in one runner passage. Fig. 4 shows the position of the sensors on the pressure side of Blade 1 and suction side of Blade 2. The signals from all the sensors were simultaneously recorded at a constant sampling frequency of 4 kHz. For more information about the measurements and the data acquisition system, see Amiri *et al.* (2015).

4. NUMERICAL METHOD

The main purpose of the numerical simulations was to determine the source of the pressure pulsations exerted on the runner while the turbine was operated at steady state. The source of the pulsations was assumed to be related to the inappropriate design of the spiral casing resulting in an asymmetric delivery of water to the runner or due to the flow condition at the spiral inlet. The flow condition in the whole turbine conduit was simulated through two separate domains to analyze the effects of each parameter on pressure pulsations exerted on the runner.

The fundamental transport equations for isothermal and incompressible fluid are considered. A general time averaging filter is applied to unsteady Navier-Stokes equations and results in the following equations:

$$\frac{\partial \bar{u}_i}{\partial x_i} = 0 \quad (1)$$

$$\rho \left(\frac{\partial \bar{u}_i}{\partial t} + \bar{u}_j \frac{\partial \bar{u}_i}{\partial x_j} \right) = -\frac{\partial p}{\partial x_i} + \frac{\partial}{\partial x_j} \left(\mu \frac{\partial \bar{u}_i}{\partial x_j} \right) - \frac{\partial (\rho \overline{u'_i u'_j})}{\partial x_j} \quad (2)$$

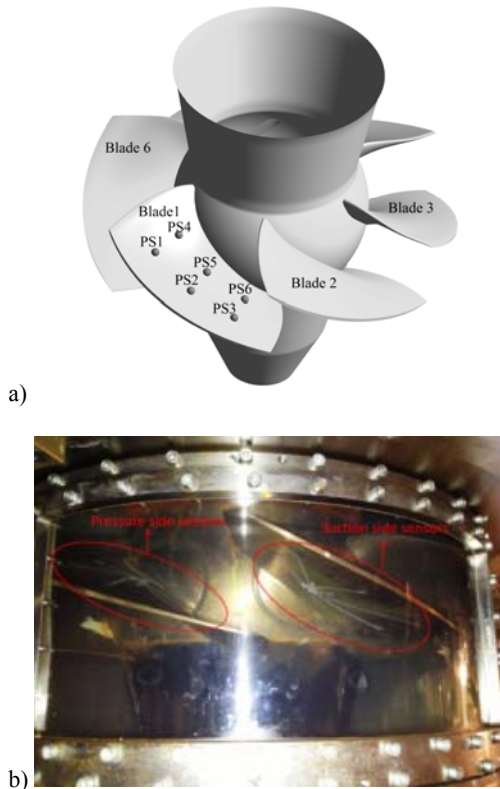


Fig. 4. The position of the pressure sensors on the suction and pressure sides of the runner blades.

where \bar{u}_i is the time-averaged velocity, u' is the velocity fluctuation, \bar{p} is the time-averaged pressure, ρ and μ are the fluid density and viscosity, respectively. The last terms on the right hand side of Eq. (2) is called Reynolds stress tensor and needs additional equations to resolve it.

The eddy-viscosity model is employed in the present work to resolve the Reynolds stress tensor. Therefore, an additional equation for calculating Reynolds stress tensor can be written as follows:

$$-\rho \overline{u'_i u'_j} = 2\mu_t S_{ij} - \frac{2}{3}\rho k \delta_{ij} \quad (3)$$

where μ_t is the turbulent viscosity, k is the mean turbulent kinetic energy and S_{ij} is the mean strain tensor. The mean kinetic energy and strain rate are defined in Eq. (4) and (5).

$$k = \frac{1}{2} \overline{u'_i u'_i} \quad (4)$$

$$S_{ij} = \frac{1}{2} \left(\frac{\partial \bar{u}_i}{\partial x_j} + \frac{\partial \bar{u}_j}{\partial x_i} \right) \quad (5)$$

In order to calculate the turbulent viscosity the Shear Stress Transport-Scale Adaptive Simulation

(SST-SAS) turbulence model is employed. In SST-SAS model, two equations for k and ω (specific dissipation rate) are solved with an additional source term in ω equation. The SAS development of SST model is based on using Von-Karman length scale for turbulence length scale and gives the capability of modeling unsteadiness to ordinary SST model.

Various initial boundary conditions were considered for the steady and unsteady simulation of different domains. The domains, meshes, and the boundary conditions are presented in section 5 and section 6.

5. COMPUTATIONAL DOMAINS AND MESHES

Flow was simulated within two computational domains to clarify the source of the pressure pulsations exerted on the runner presented by Amiri *et al.* (2015). The first domain comprised the parts located upstream of the distributor of the model: the complete upstream tank of the test rig incorporated with the penstock and the volute of the model (water supply system domain). The second domain included different parts of the turbine from the inlet of the spiral casing to the draft tube outlet (turbine domain).

5.1 Water supply system domain

Initial investigations by Mulu and Cervantes (2010) showed that the flow condition at the inlet of the spiral casing of Porjus U9 model is far from the ideal case of a fully developed pipe flow. Their measurements showed the presence of Dean-like vortices at the measurement location due to the upstream bend in the penstock, resulting in an inhomogeneous axial flow and vortical flow structures at the inlet of the spiral casing.

Refined LDA measurements were performed to investigate the flow condition at the inlet of the spiral casing to use the results as the inlet boundary condition for the “Turbine domain”. However, the 2D LDA measurements do not provide any information about the radial component, making it impossible to predict the structure of the secondary flows at the measurement section. Such structures may disturb the flow condition within the spiral casing and affect its performance. Hence, the flow was simulated within the penstock to capture the secondary flow structures and the radial velocity. The LDA results were used to validate the numerical simulations.

The numerical simulations of the penstock showed that the flow condition at the inlet of the spiral casing is influenced by the interaction between the penstock, upstream tank, and the spiral casing. Hence, these parts were included in the simulations. Fig. 5 shows different parts incorporated to form the water supply system domain: the upstream tank in orange, the penstock in blue and the spiral casing in green.

The domain was composed of four mesh regions generated separately using ICEM CFD 16.0. A

comparably course tetra mesh comprising ~147,000 nodes and ~822,000 elements with higher densities close to the funnel of the penstock was used to simulate the flow within the tank. The mesh is shown in Fig. 6. The main interest in simulating the flow inside the tank was to approximate the flow condition at the inlet of the penstock instead of considering the mass flow rate as the inlet boundary condition of the penstock.

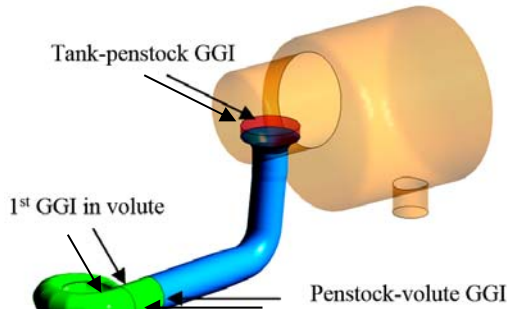


Fig. 5. Different parts of the water supply system domain. Orange: upstream tank, blue: penstock, green: spiral casing, red: GGI between the upstream tank and the penstock.

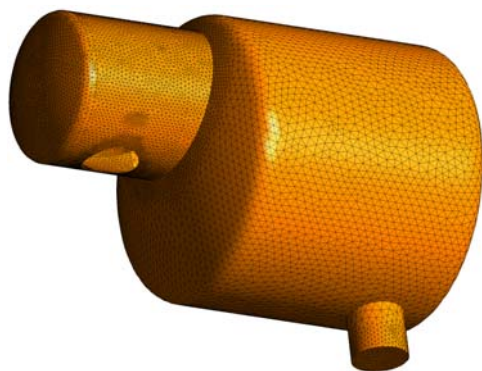


Fig. 6. The geometry of the upper tank together with the tetra mesh.

A high-quality hexahedral mesh with 1.9 million nodes was generated inside the penstock and the funnel connecting it to the upper tank. The y^+ parameter was kept near unity to resolve the boundary layer. The minimum angle achieved in the mesh was 28.3° , which is higher than the recommended value of 20° for CFD simulations. Fig. 7 shows the penstock mesh. A modified asymmetric O-grid with an octagonal core was considered for meshing the penstock because of the asymmetries in the geometry of the spiral casing. The penstock mesh was interfaced with the tank mesh through a GGI. The GGI was cylindrical and located on top of the funnel at the penstock entrance instead of a simple circular one to increase the mesh quality close to the interface area. The geometric angle approached zero at the funnel entrance, decreasing the mesh minimum angle to the geometrical value when using a circular interface at this location.

The spiral casing mesh was divided into three hexahedral mesh regions connected to each other through planar GGIs. The mesh was composed of approximately 2.1 million nodes. A few elements had an orthogonal angle less than 20° , with a minimum angle of 18.6° . The maximum y^+ was 40. The spiral casing was connected to the penstock through a planar GGI as well. The cross section of the spiral casing mesh is presented in Fig. 8.

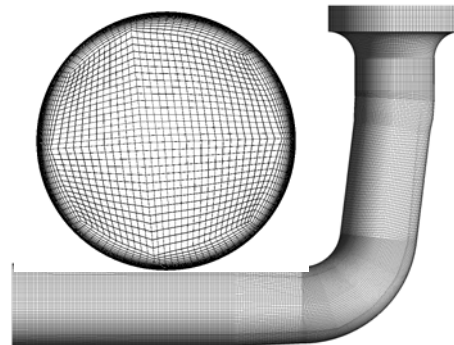


Fig. 7. Cross section and the side view of the penstock mesh.

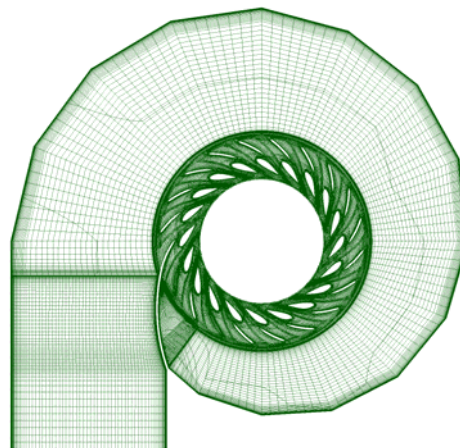


Fig. 8. Cross section of the mesh, generated inside the spiral casing and distributor.

5.2 Turbine Domain

The “turbine domain” incorporated all parts of the turbine model, including the volute; the distributor, which features 18 stay vanes and 20 GVs; the six-bladed Kaplan runner; and the elbow-type draft tube. This study focused on the interaction between the distributor and the runner.

The mesh generated for the volute to simulate the flow within the “water supply system domain” was used for this simulation as well. The distributor consisted of three types of water passages: two passages with only one GV (type one), seventeen passages incorporating a GV and a stay vane (type 2), and one passage with a GV and an extended stay vane operating as the tongue of the volute entrance (type 3); see 0a. Each passage featured a separate mesh, and the meshes were connected to each other through GGIs at their interfaces, forming the whole distributor. The mesh quality was

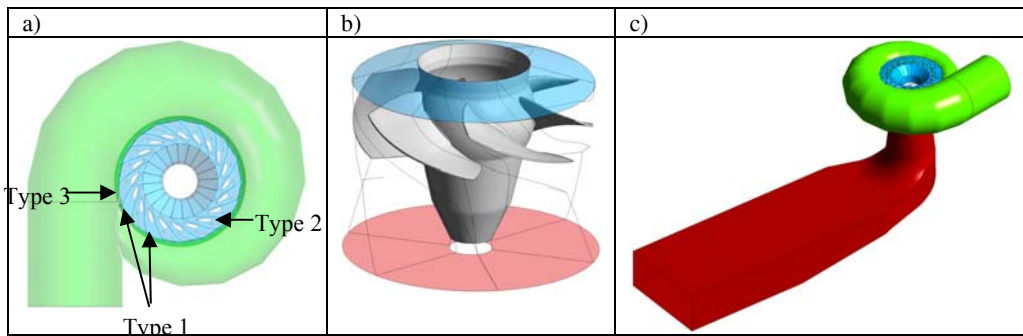


Fig. 9. Sketch of different parts of the turbine domain: a) volute and the distributor, b) runner and c) the whole domain.

improved by using this method from a minimum mesh angle perspective. The minimum angle achieved in the distributor mesh was 20° . All specific features of the geometry in the distributor, including the overhang region, were considered during meshing. Fig. 10 shows the meshes generated for each passage type. The distributor was connected to the volute through a GGI. The distributor mesh was composed of 4.3 million nodes. The maximum y^+ in the distributor was 80.

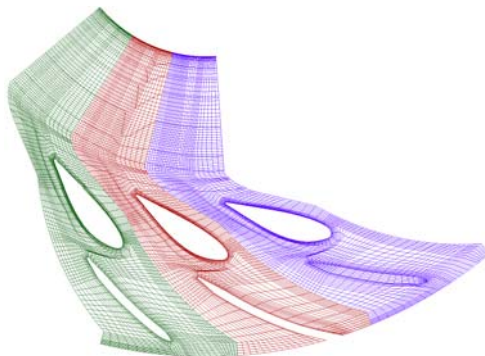


Fig. 10. The three types of the mesh in the distributor; violet: type 1 (see Fig. 9a), green: type 2, red: type 3.

The runner blades were scanned using a 3D optical scanning apparatus (ATOS III system from GOM) with an accuracy of ± 0.03 mm. A procedure similar to that used for meshing the distributor passages was considered for meshing the runner blade passages. The runner was composed of six identical runner blades. One passage was meshed using hexahedral elements, and the mesh was transformed and copied to form the whole runner. The minimum angle achieved was 16.8° . The mesh included all features of the geometry, including hub and tip clearances; see Mulu *et al.* (2015). A GGI was used at the interface between each two adjacent mesh regions. The runner mesh was composed of 2.7 million nodes, and y^+ was kept below 200 in the runner mesh region. A sketch of the runner is presented in Fig. 9b. The runner is shown in gray, whereas the runner interfaces with the distributor and the draft tube are indicated by the blue and orange surfaces, respectively. The corresponding mesh is presented in Fig. 11.

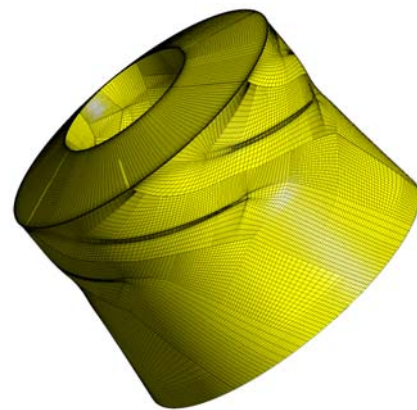


Fig. 11. The generated mesh over the runner domain.

The runner was followed by the elbow-type draft tube shown in red in Fig. 9c. The draft tube exit was extended by a 2 m long straight duct, and the outlet boundary condition was applied at the end of the duct. This is a standard procedure implemented in the simulation of draft tubes for the sake of convergence of the numerical simulations. The value of y^+ was kept close to unity in the draft tube mesh. The number of nodes in the draft tube mesh was 3.7 million. The mesh is shown in Fig. 12. A GGI was used as an interface between the rotating runner mesh and the draft tube mesh.



Fig. 12. The generated mesh within the draft tube.

6. SIMULATIONS

The commercial software ANSYS-CFX-16.0 was used in this study. The governing equations were the continuity and momentum equations for incompressible flows. The simulation methods and parameters considered in simulating the water supply system domain and the turbine domain are presented in the following sections.

6.1 Water Supply System Domain

Unsteady Reynolds-averaged Navier-Stokes equations (URANS) were solved considering incompressible flow. Flow within the penstock of the case study may undergo unsteadiness and flow separation due to the penstock bend, followed by a slightly diverging section. The Scale-Adaptive Simulation based on Shear Stress Transport (SAS-SST) model was used for turbulence modeling for the sake of closure of the equations. The SAS method is an improved URANS formulation, with the ability to adapt the length scale to resolve turbulent structures, resulting in LES-like behavior in unsteady regions of the flow field. The model provides standard RANS capabilities in stable flow regions. The SST model accounts for the transport of the turbulent shear stress and yields highly accurate predictions of the onset and the amount of flow separation under adverse pressure gradients.

The mass flow rate measured during the experimental investigation of the test case was considered as the inlet boundary condition to the inlet pipe of the upstream tank: $Q=0.7 \text{ m}^3/\text{s}$. A medium turbulence intensity of 5% was considered for the flow entering the tank. It is expected that this parameter does not affect the flow condition within the penstock due to the presence of the upstream tank. Flow at the outlet of the volute showed complex features comprising reverse flows. Hence, an “opening” boundary with 5% turbulence intensity was considered at the outlet of the volute, allowing for reverse flow to the domain. A relative pressure of zero Pascal was applied at this section. All the walls were considered to be smooth with a no-slip condition. An automatic near-wall function was employed for the treatment of the boundary layer. This feature automatically switches from wall functions to a low-Re near-wall formulation as the mesh is refined. Thus, flow is resolved in the near-wall region of the penstock, which is the main focus for this simulation.

“High resolution” was chosen for both the advection scheme and turbulence modeling in the solver. This scheme employs a blend factor that varies throughout the domain between second- and first-order accuracy based on the local solution field to avoid non-physical oscillations. The implicit time stepping of the second-order backward Euler method was implemented for the transient scheme, which is the recommended scheme for transient simulations in CFX.

The simulation started with a steady-state simulation of the domain using the SST turbulence model. The steady-state simulation result was

considered as the initial guess to initiate the unsteady SAS-SST simulations. The transient simulation was run for 30 s with a time step of 0.01 s. The results were averaged over the last 10 s of the simulation when the flow was supposed to be developed inside the domain to present the average flow condition.

6.2 Turbine Domain

The SAS-SST model was used to simulate the turbine model with advection, transient, and turbulence modeling schemes similar to those used for simulation of the water supply system domain. Two types of inlet boundary conditions were used at the inlet of the spiral casing: a mass flow rate of $0.7 \text{ m}^3/\text{s}$ and the result of the numerical simulations from the water supply system domain at the inlet of the spiral casing. Using these conditions allowed for the investigation of the effect of the penstock geometry on the flow condition within the turbine and, more specifically, the interaction between the distributor and the runner.

The simulations began with a steady-state simulation of the turbine considering a frozen rotor at the interface between the runner domain and stationary domains located up- and downstream. The SST turbulence model was employed for the steady-state simulation. The result of the frozen rotor simulation was considered as the initial guess of the transient simulation, which employed a transient rotor-stator simulation at the interfaces between the runner and the stationary domains. The time step during the simulation was 0.239 ms, corresponding to approximately 1° of runner rotation. The simulation was run for approximately 2.7 s, corresponding to approximately 30 runner revolutions.

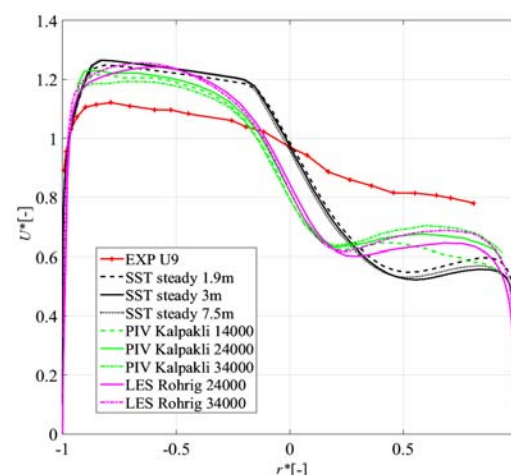


Fig. 13. Numerical and experimental results at the inlet of spiral casing together with the results of Kalpakli and Örlü (2013) and Röhrig *et al.* (2015).

7. RESULTS AND DISCUSSIONS

7.1 Water Supply System Results

Flow within the water supply system of the turbine

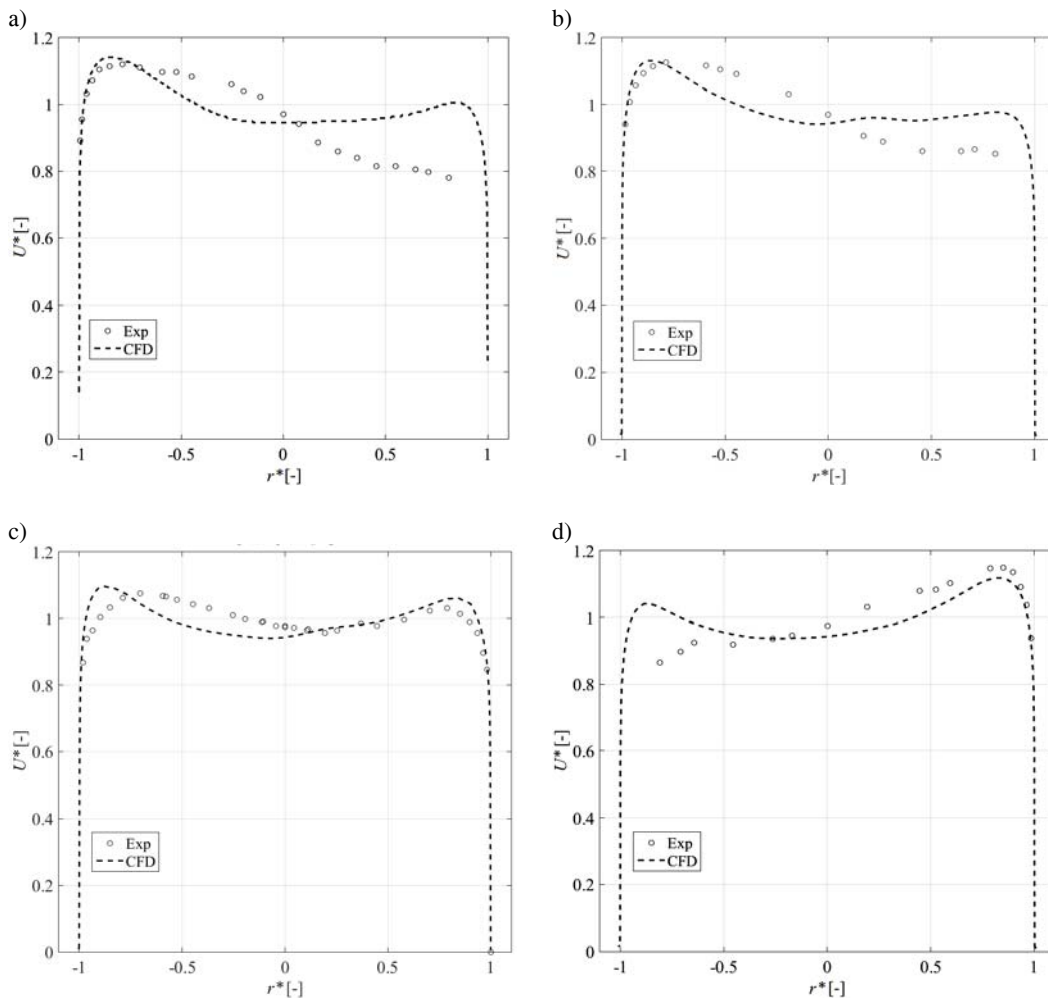


Fig. 14. Streamwise velocities from experiments and CFD simulations: a) Line A, b) Line B, c) Line C-G, and d) Line H.

model was simulated to find the appropriate boundary condition that should be implemented at the inlet of the spiral casing for the numerical simulation of the turbine. Investigations of the flow condition within the penstock began with a simulation of the penstock together with the straight section of the volute, i.e., inlet of the spiral casing to the location of the “1st GGI in volute” shown in Fig. 5. Three different meshes with 1.9, 3 and 7.5 million nodes in the penstock were used for mesh sensitivity analysis using the SST model. The results of the streamwise velocity along Line A (shown in 0Fig. 3) are presented in 0Fig. 13. The figure also shows the streamwise velocity distribution after a pipe bend implementing PIV measurements (Kalpakli and Örlü, 2013) and LES simulations (Röhrig *et al.*, 2015) of the case for comparison. The numbers in the legend of the figure represent the mesh size used for this study and the Reynolds number used during measurements and LES simulations. Two conclusions can be drawn from the results. First, the simulation results are independent of the mesh size when a mesh containing more than 1.9 million is used for the simulation. Second, the numerical simulation results are qualitatively similar to the

PIV measurements of Kalpakli and Örlü (2013) and the LES simulations of Röhrig *et al.* (2015). The quantitative differences can be explained by the difference in Reynolds numbers, and the difference in geometries and measurement locations between the current one and the ones presented in the references. However, the LDA results do not follow the variations in the current numerical simulations or those presented in the references. This finding suggests that the flow within the penstock is different from Dean-vortex-dominated flow after a pipe bend. Hence, it was concluded that the disturbances from either downstream or upstream components distort the flow within the penstock. The stationary components located after the penstock, i.e., the volute and distributor, were added to the domain; however, this placement did not affect the results at the LDA measurement section. Including the upper tank in the computational domain drastically affected the flow condition within the penstock.

Figure 14 compares the streamwise velocity components obtained from CFD simulations with those acquired by LDA measurements. Adding the upper tank solved the problem associated with the

high gradient of the streamwise velocity close to the pipe center. One of the main differences between the CFD and experimental results is the annular distribution of the streamwise velocity captured by the CFD simulations in sections Line A, Line B and Line H, which cannot be observed in the experimental data. In other words, the CFD results showed an increase in streamwise velocity close to the penstock walls, whereas the experimental results showed a decrease close to $r^*=1$ at sections Line A and Line B and close to $r^*=-1$ at Line H. Because the main phenomena resulting in such an annular flow distribution are the centrifugal forces exerted on the flow by vortices inside the flow, it can be concluded that the numerical simulations overestimated the strength of the vortices at this section. This overestimation may have been due to either the performance of the turbulence model used for the simulations or the simulation of flow inside the flow upstream tank. As previously mentioned, a course tetra mesh was used to simulate the flow inside the tank, which may have affected the flow condition at the inlet of the penstock. Further investigation of these parameters is required to enhance the quality of the results. However, the results can still be used to study the effect of the flow condition entering the spiral casing on the flow condition within the volute and the distributor for the sake of sensitivity analysis.

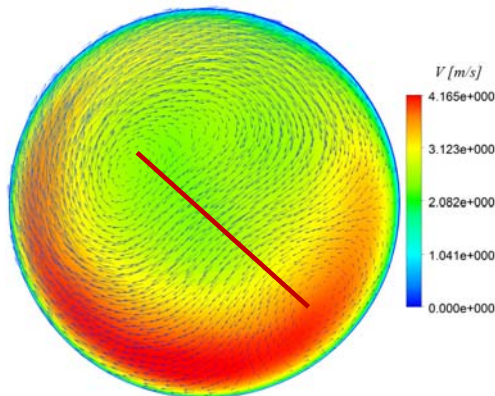


Fig. 15. Contour of the streamwise velocity together with the corresponding in-plane vector map at the inlet of spiral casing. The red line connects the centers of the vortices.

The contour of the streamwise velocity together with the corresponding in-plane vector map in the LDA measurement section is presented in Fig. 15. The main flow features are qualitatively similar to those after a pipe bend: two counter-rotating vortices identical to Dean vortices after a pipe bend are clearly visible at this location, and flow is pushed towards the penstock walls. However, certain differences exist between the two cases. The symmetry of the Dean vortices is distorted at this location, and the axis connecting the centers of the vortices, indicated by a red line in Fig. 15, is not horizontal. The asymmetry between the right and left halves of the penstock can also be observed in the contour of the axial velocity. The fact that the asymmetry was introduced into the penstock after

considering the upstream tank in the computational domain confirms that the asymmetry was caused by the non-homogeneous flow fed to the penstock by the upstream tank. Fig. 16 shows a top view of the location where the penstock was connected to the tank through a bell-mouth. The contour and the vector map show the contour of the streamwise velocity and the corresponding in-plane vector map at the inlet of the penstock. It is worth noting that the axis of the tank was rotated by approximately 8.2° with respect to the axis of the penstock.

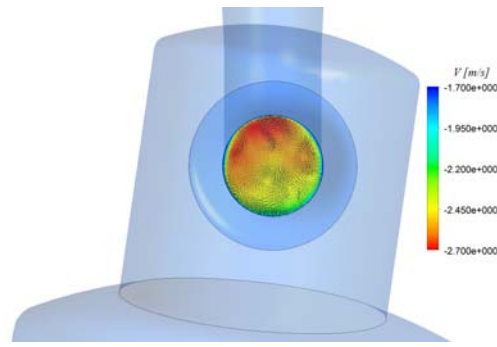


Fig. 16. The contour of the streamwise velocity together with the corresponding in-plane vector map at the inlet of the penstock.

7.2 Turbine Model Results

Two different velocity profiles were applied to the inlet of the spiral casing: plug flow and the results from the simulation of the water supply system domain. Fig. 17 illustrates contours of velocity at the mid-section of the GVs together with the vector maps in two GV channels: one with flow separation and one without separation. The flow conditions within the distributor were similar when plug flow or the CFD result obtained from the water supply system simulation was used as the inlet boundary condition. In both cases, flow separation was captured on stay vanes 2 to 7. This is in agreement with the pressure fluctuations captured on the blades of the runner reported by Amiri *et al.* (2015), where the results showed significant pressure fluctuations with respect to the GV/SV passing frequency on the runner for about 100° rotation of the runner.

Figure 18 presents the velocities and flow angle profiles upstream of the stay vanes and at the mid-height section of the distributor. The velocity components are presented in the cylindrical coordinate system where the axial component is aligned with the turbine axis; U_θ , U_r , and U_{ax} represent the circumferential, radial and axial velocities, respectively. The horizontal axis shows the circumferential position, θ , which is shown in Fig. 17a. The flow angle is defined as the angle between the circumferential velocity and the velocity vector. The lip-entrance junction of the volute is represented by a sudden change in the profiles in each figure at approximately $\theta=340^\circ$. As shown in the figure, changing the inlet boundary condition does not have any distinctive effect on either the flow angle or the radial and

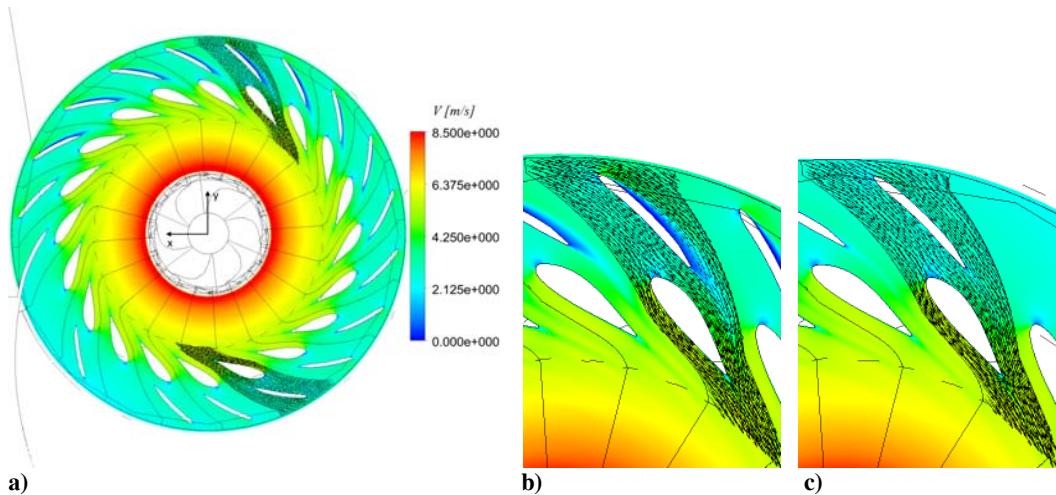


Fig. 17. a) Velocity contours at the mid-volute section while plug flow is considered as inlet boundary condition to the spiral casing; b) flow conditions around GV number 6 (with separation) and c) flow conditions around GV number 16 (without separation).

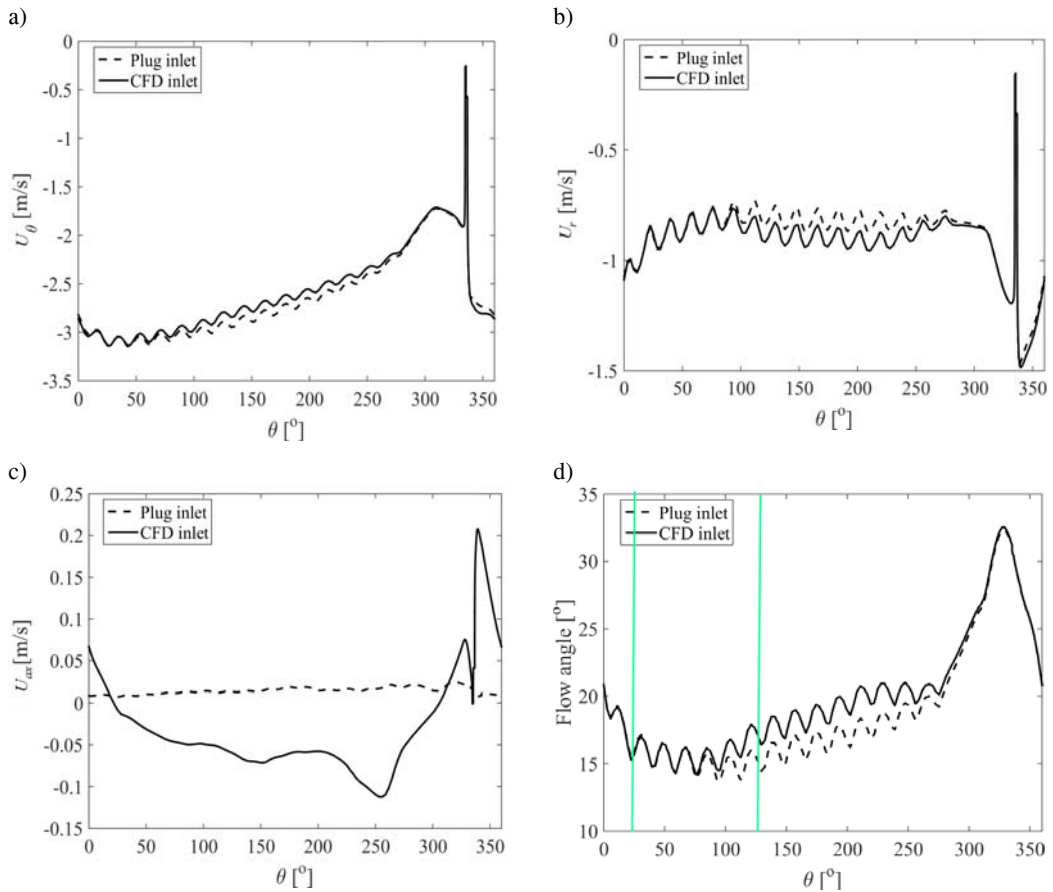


Fig. 18. Velocity profiles and flow angle at the inlet of the distributor.

circumferential velocity components. However, the axial velocity profiles are different between these cases. The axial velocity is nearly zero in the case in which a straight plug flow is used as the inlet boundary condition, whereas it is almost negative along the entire circumference of the volute in the case in which the CFD simulation results are used as the inlet boundary condition. This finding

demonstrates that the swirling flow structure implemented as the inlet boundary condition (see Fig. 15) influences the flow in the whole circumstance of the volute. However, the flow condition downstream of this location, i.e. within the distributor shown in Fig. 17, shows that the axial component of the velocity at the distributor inlet does not affect the flow condition within the distributor.

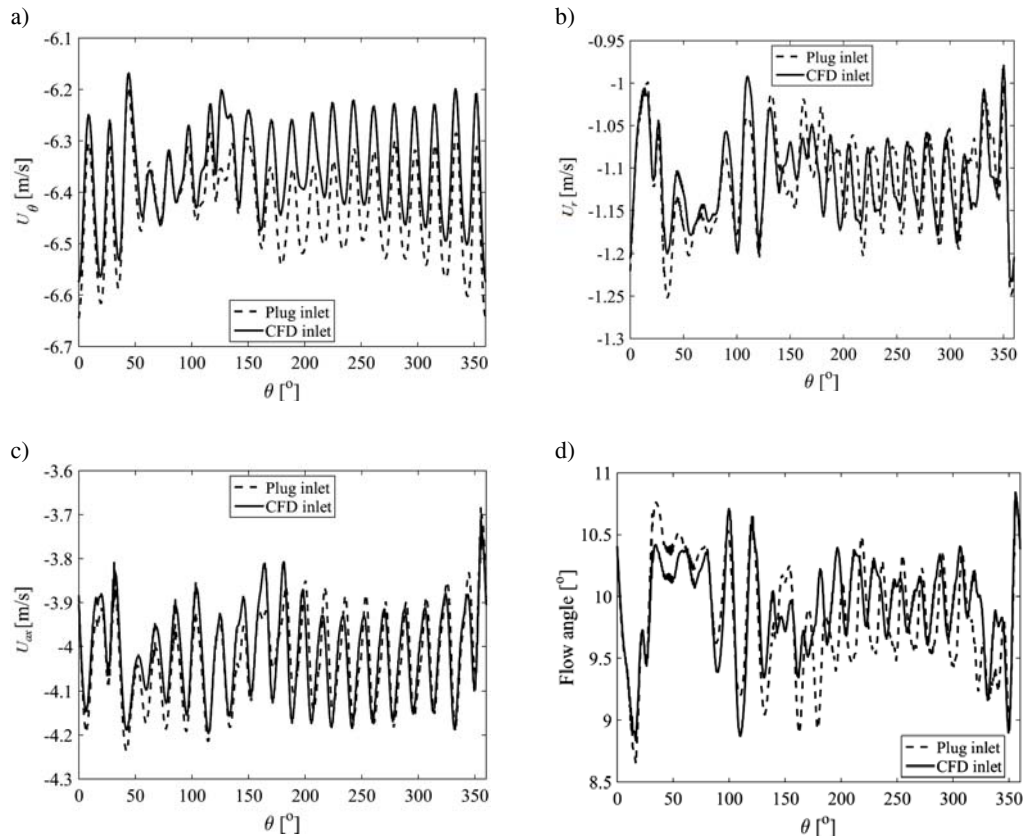


Fig. 19. Velocity profiles and flow angle at the inlet of the runner.

Figure 18d shows variations in the flow angle in the circumference of the volute. The two vertical green lines indicate the circumferential interval where the flow separates on the SVs. The lower flow angle at this location compared with the angles at the other circumferential locations causes a high angle of attack on the stay vanes, and ultimately, the flow is separated on the suction side of the stay vanes located close to this circumferential position. Optimizing the volute to prevent such flow asymmetry at the inlet of the distributor can always be considered as an option to improve flow symmetry delivered to the distributor and decrease flow losses associated with flow separation. However, because the flow is separated on the stay vanes by changing the angle of attack by only $\sim 3^\circ$ (see Fig. 18d), another alternative can be replacing the current stay vanes with more hydraulically shaped ones using hydrofoils with a higher thickness-to-chord ratio. This option is more feasible for already manufactured turbines because it does not require design optimization of the spiral casing or modifying water supply systems that typically are not refurbished in power plants.

The velocity profiles together with the flow angle profile at the inlet of the runner are presented in Fig. 19. As shown in the figures, the inlet boundary condition does not have any distinct effect on the magnitude of the velocity or flow angle fluctuations at the inlet of the runner.

Figure 20 presents amplitude spectra of the pressure signals from the sensors located on the suction and pressure sides of the runner blades, whereas the two different inlet boundary conditions are used for the simulations. The figure presents the results obtained from sensors located close to the shroud of the runner near the leading and trailing edges of the blades, PS1, PS3, SS1 and SS3 shown in Fig. 4. In both simulations, the distinct frequencies in the spectra were the runner frequency and its harmonics. Similar results were obtained at the other sensors located on the runner blades. The results show that changing the velocity distribution at the inlet of the spiral casing due to the simulation of water supply system does not have any noticeable effect on the pressure fluctuations exerted on the runner. The results demonstrate that the dominant frequency is the runner frequency attributed to the variable flow angle and velocity magnitude at the inlet of the runner because of different signature for each guide vane wake.

Waterfall plots of the pressure signals obtained from all the pressure sensors on the runner blades from the numerical simulations as well as experimental investigations of Amiri *et al.* (2015) are presented in Fig. 21. The results presented in Fig. 21a are the ones that were acquired from the numerical simulations using the CFD results at the inlet of the spiral casing. The results show that the frequencies are estimated accurately in the

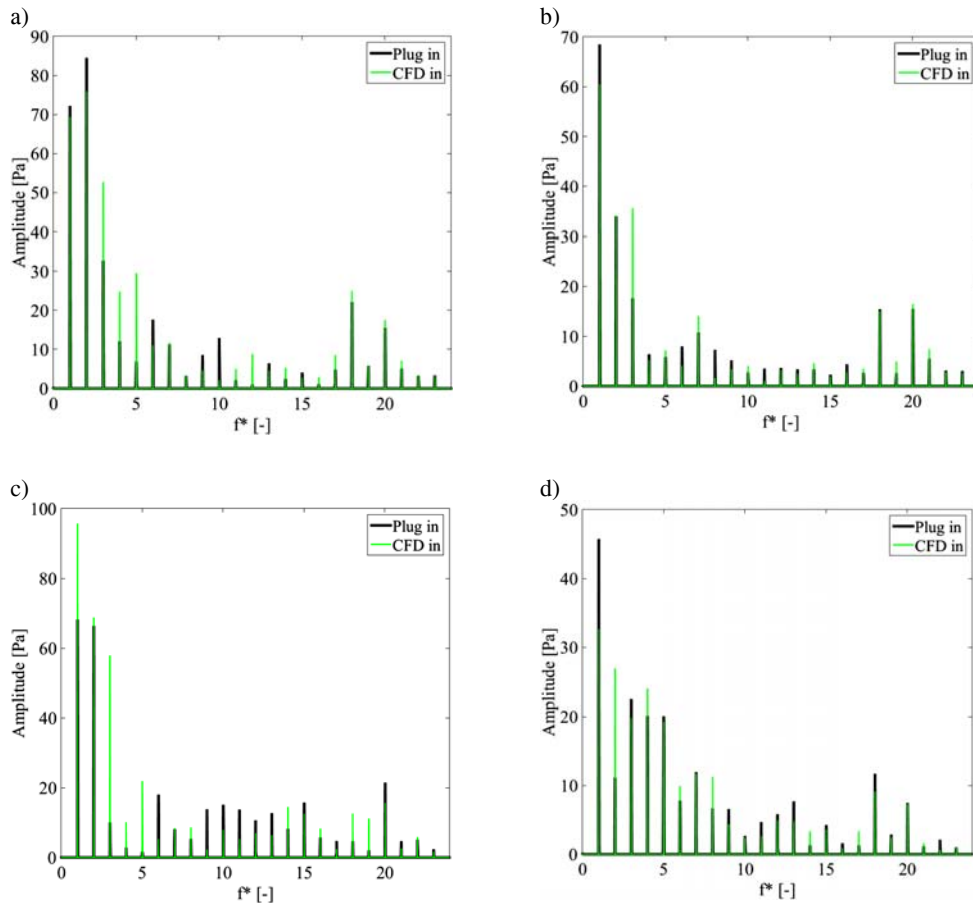


Fig. 20. Amplitude spectra of pressure signals from the sensors located on the runner blades: a) PS1, b) PS3, c) SS1, and d) SS3.

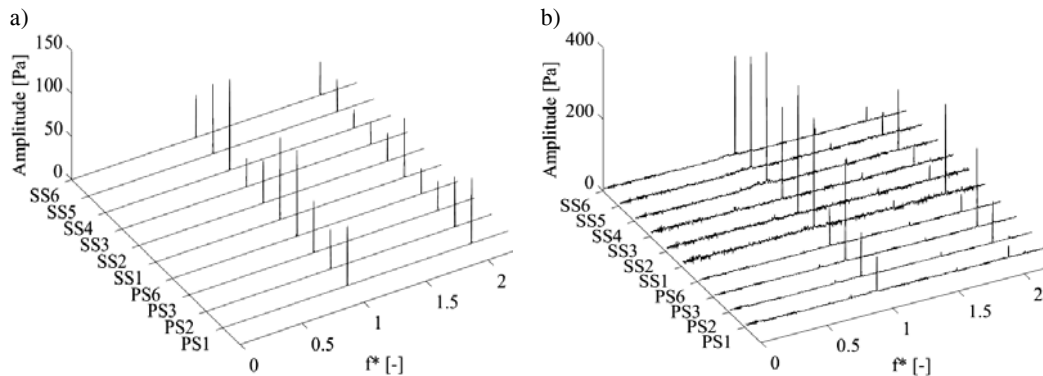


Fig. 21. Waterfall plots of pressure sensors located on the runner: a) CFD simulations and b) experimental results from Amiri *et al.* (2015). The scales of the vertical axes are different in the two waterfalls.

numerical simulations; however, the corresponding amplitudes are not. The amplitudes estimated by the numerical simulations are approximately one-third of the amplitudes determined experimentally. This discrepancy can be related to either the early dissipation of the wakes traveling downstream from the distributor due to the turbulence modeling and numerical dissipation or to the mesh density, which may not be appropriate in the distributor or the runner regions.

8. CONCLUSIONS

Numerical simulations were performed to investigate the flow condition within the water supply system of the Porjus U9 model as well as within the turbine, and the results were validated against LDA and pressure measurement results. CFD simulations of the water supply system, including the upstream tank, the penstock, and the volute, showed that inhomogeneous flow with

swirling structures was fed to the inlet of the spiral casing, in agreement with the LDA measurements performed at this location. Investigations demonstrated that the asymmetric flow fed by the upstream tank to the penstock affected the flow condition within the penstock and that at the inlet of the spiral casing. Hence, the inclusion of the upstream tank was essential for the flow simulation. Two inlet boundary conditions were implemented at the inlet of the spiral casing for flow simulation within the model to investigate flow sensitivity within the turbine and pressure fluctuations in particular on the runner blades to the inlet boundary condition. The results showed that the inlet boundary condition does not have any distinctive effect on the flow condition within the volute and the distributor. In both cases, flow was separated on the suction side of stay vanes 2 to 7. This resulted in an asymmetrical flow fed to the runner by the spiral casing and wake propagation from the GVs to the runner. This increased the level of the rotor-stator interaction and resulted in pressure fluctuations exerted on the runner at the runner frequency and guide vanes passing frequency. The dominant frequencies were estimated accurately based on the amplitude spectra of the pressure fluctuations exerted on the runner blades. However, the corresponding amplitudes were underestimated by a factor of approximately 3. The preliminary results showed that numerical simulations are capable of predicting the effect of flow asymmetry at the distributor outlet of the model on pressure fluctuations exerted on the runner blades. However, further investigations are required to study the effect of the mesh quality and the modeling techniques on the results.

REFERENCES

- Amiri, K., M. J. Cervantes and B. Mulu (2015). Experimental Investigation of the Hydraulic Loads on a Kaplan Turbine Runner Model and Corresponding Prototype. *J. of Hydraulic Research* 53(4), 452-465.
- Farhat, M., F. Avellan and U. Seidel (2002). Pressure fluctuation measurements in hydro turbine models. *9th International Symposium on Transport Phenomena and Dynamics of Rotating Machinery*. Honolulu, Hawaii, USA.
- Fortin, M., S. Houde and C. Deschênes (2014). Validation of simulation strategies for the flow in a model propeller turbine during a runaway event. *27th IAHR Symposium on Hydraulic Machinery and Systems*, Montreal, Canada.
- Gagnon, J. M., C. Deschenes and G. D. Ciocan (2008). Numerical simulation and experimental investigation of the flow in an axial turbine. *24th IAHR Symposium on Hydraulic Machinery and Systems*, Foz Do Iguassu, Brazil.
- Javadi, A. and H. Nilsson (2014). Unsteady numerical simulation of the flow in the U9 Kaplan turbine model. *27th IAHR Symposium on Hydraulic Machinery and Systems*, Montreal, Canada.
- Kalpakli, A. and R. Örlü (2013). Turbulent Pipe Flow Downstream a 90° Pipe Bend with and without Superimposed Swirl. *International Journal of Heat and Fluid Flow* 41, 103-111.
- Kobro, E. (2010). *Measurement of Pressure Pulsation in Francis Turbines*. PhD thesis, Norwegian University of Science and Technology (NTNU), Trondheim, Norway.
- Kolsek, T., J. Duhovnik and A. Bergant (2006). Simulation of Unsteady Flow and Runner Rotation during Shut-Down of an Axial Water Turbine. *Journal of Hydraulic Research*, 44(1), 129-137.
- Kumar, D. and P. P. Bhingole (2015). CFD Based Analysis of Combined Effect of Cavitation and Silt Erosion on Kaplan Turbine. *Materials Today: Proceedings* 2, 2314-2322.
- Liu, S., D. Zhou and D. Liu (2010). Runaway Transient Simulation of a Model Kaplan Turbine. *Earth and Environmental Science* 12, 012073.
- Liu, S., S. Jie and S. Wu (2008). Numerical Simulation of Pressure Fluctuation in Kaplan Turbine. *Science in China Series E: Technological Sciences* 51(8), 1137-1148.
- Liu, S., S. Li and Y. Wu (2009). Pressure Fluctuation Prediction of a Model Kaplan Turbine by Unsteady Turbulent Flow Simulation. *Journal of Fluids Engineering* 131, 1-9.
- Mulu, B. (2012). *An Experimental and Numerical Investigation of a Kaplan Turbine Model*. PhD thesis, Luleå University of Technology, Luleå, Sweden.
- Mulu, B. G., M. J. Cervantes and C. Devals (2015). Simulation-Based Investigation of Unsteady Flow in Near-Hub Region of a Kaplan Turbine with Experimental Comparison. *Engineering Application of Computational Fluid Mechanics* 9(1), 139-156.
- Mulu, B. and M. Cervantes (2010). LDA Measurements in a Kaplan Spiral Casing Model. *13th Symposium on Transport Phenomena and Dynamics of Rotating Machinery*, Honolulu, Hawaii, USA.
- Nennemann, B. and T. C. Vu (2007). Kaplan turbine blade and discharge ring cavitation prediction using unsteady cfd. *2nd IAHR International Meeting of the Workgroup on Cavitation and Dynamic Problems in Hydraulic Machinery and Systems*, Timisoara, Romania.
- Nicolle, J., P. Labbe and M. Gauthier (2010). Impact of blade geometry differences for the CFD performance analysis of existing turbines. *IOP Conf. Series: Earth and Environmental Science*, Timisoara, Romania.
- Petit, O., B. G. Mulu and O. Nilsson (2010). Comparison of numerical and experimental results of the flow in the U9 Kaplan turbine model. *25th IAHR Symposium on Hydraulic*

- Machinery and Systems*, Timisoara, Romania.
- Röhrig, R., S. Jakirlić and C. Tropea (2015). Comparative Computational Study of Turbulent Flow in a 90° Pipe Elbow. *International Journal of Heat and Fluid Flow* 55, 120-131.
- Trivedi, C., M. J. Cervantes and B. K. Gandhi (2016). Investigation of a High Head Francis Turbine at Runaway Operating Conditions, *Energies* 9(3), 1-22.
- Trivedi, C., M. J. Cervantes and B. K. Gandhi (2013). Experimental and Numerical Studies for a High Head Francis Turbine at several Operating Points, *Journal of Fluids Engineering*, 135(11), 1-17.
- Trivedi, C., B. K. Gandhi and M. J. Cervantes (2015). Experimental Investigations of a Model Francis Turbine during Shutdown at Synchronous Speed. *Renewable Energy* 83, 828-836.
- Trivedi, C., M. J. Cervantes and O. G. Dahlhaug (2015). Experimental Investigation of a High Head Francis Turbine during Spin-no-Load Operation, *Journal of Fluids Engineering*, 137(6), 1-10.
- Vu, T. C., M. Koller and M. Gauthier (2010). Flow simulation and efficiency hill chart prediction for a Propeller turbine. *IOP Conf. Series: Earth and Environmental Science*, Timisoara, Romania.
- Wu, Y., S. Liu and H. Dou (2012). Numerical Prediction and Similarity Study of Pressure Fluctuation in a Prototype Kaplan Turbine and the Model Turbine. *Computers and Fluids* 56, 128-142.